Electronic Supplementary Material (ESI) for Lab on a Chip.
This journal is © The Royal Society of Chemistry 2019

Supplementary Information

Self-sufficient, low-cost microfluidic pumps utilising reinforced balloons

Peter Thurgood [1,†], Sergio Aguilera Suarez [1], Sheng Chen [1], Christopher Gilliam [1], Elena Pirogova [1], Aaron R. Jex [2,3], Sara Baratchi [4,*], Khashayar Khoshmanesh [1,*,†]

[1] School of Engineering, RMIT University, Melbourne, Australia

[2] Population Health and Immunity Division, The Walter and Eliza Hall Institute of Medical Research, Parkville, Australia

[3] Faculty of Veterinary and Agricultural Sciences, The University of Melbourne, Parkville, Australia

4 School of Health & Biomedical Sciences, RMIT University, Bundoora, Australia

* These authors contributed equally.

† **Corresponding authors:**

Peter Thurgood: peter.thurgood@rmit.edu.au

Khashayar Khoshmanesh: Khashayar.khoshmanesh@rmit.edu.au

Supplementary Information 1: Assembly process of the reinforced balloon pumps

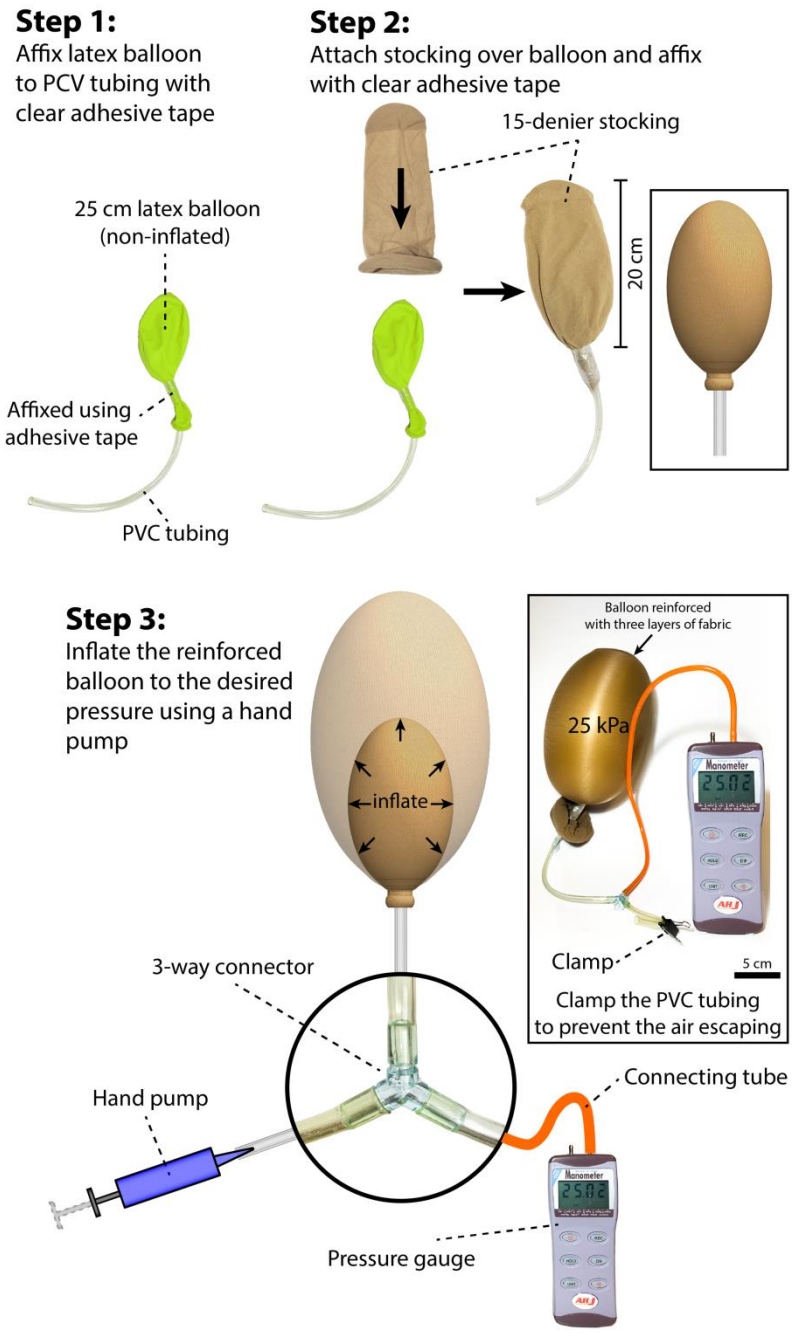

Figure S1. The process of assembling of the reinforced balloon, consisting of three major steps: Step 1: A latex balloon is affixed to a section of PVC tubing with removable adhesive tape. Step 2: A stocking is then placed over the balloon and affixed to the PVC tubing. Step 3: The assembled reinforced latex balloon is coupled with a digital pressure gauge and a manual hand pump via PVC tubing and a 3-way hose connecter for inflation.

Supplementary Information 2: Experimental setup

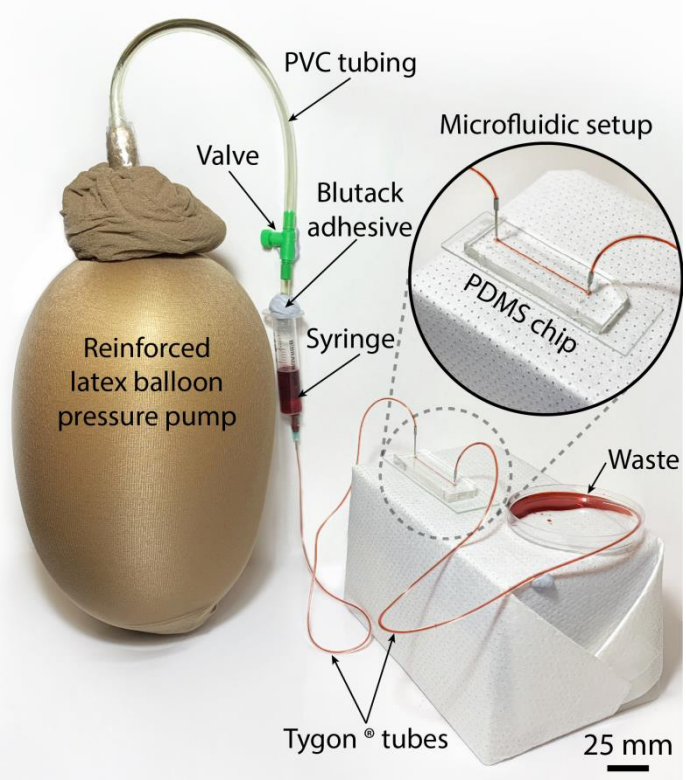

Figure S2. Experimental setup of the reinforced balloon pump consisting of (i) a reinforced latex balloon, (ii) connected to a liquid filled syringe, (iii) using PVC tubing, (iv) with an optional 2-way valve, (v) interfaced with a PDMS based microfluidic structure, (vi) using Tygon® tubing.

Supplementary Information 3: Detailed geometry of microfluidic structures used in the manuscript

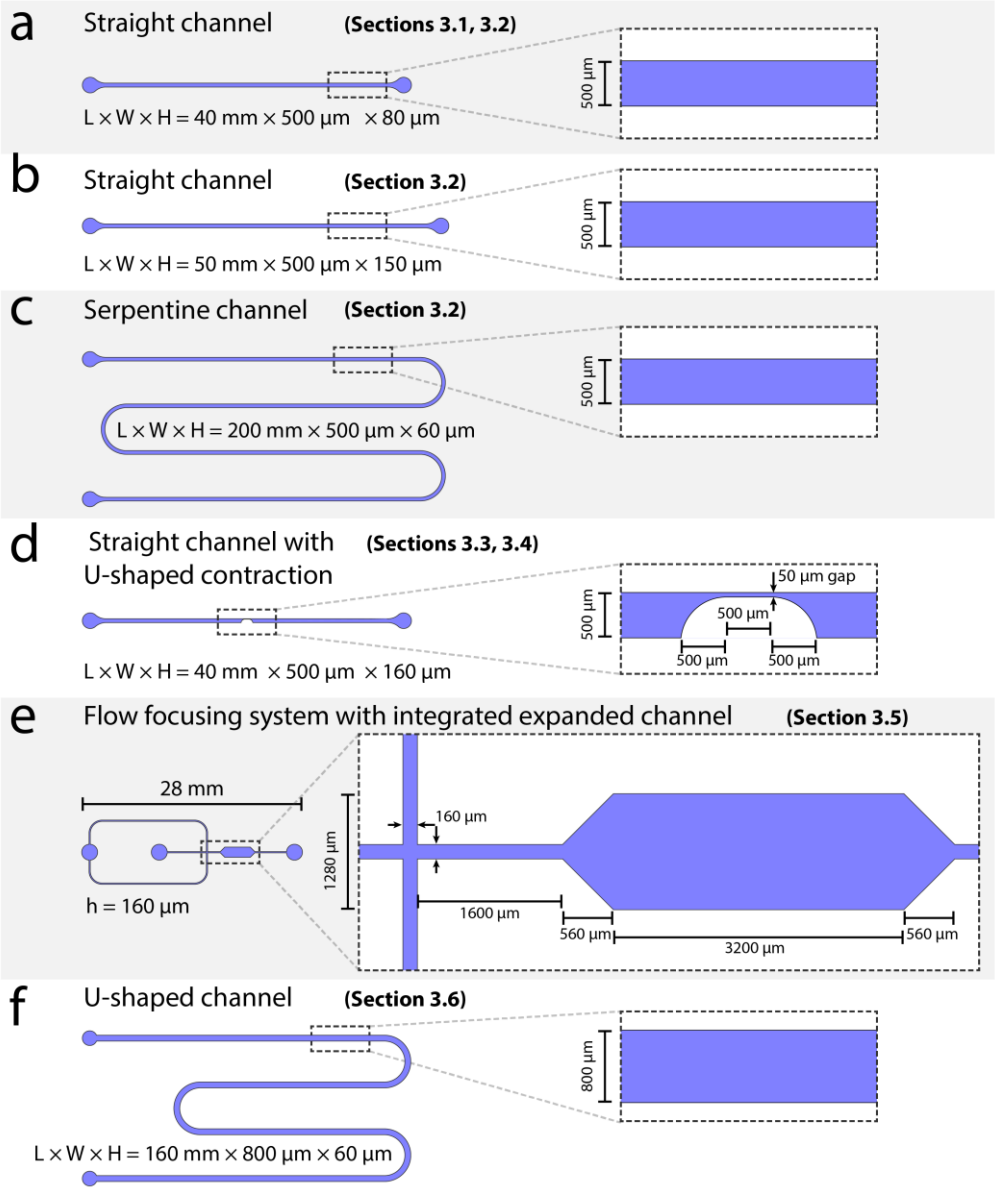

Figure S3. Detailed geometry of the microfluidic structures used in our work, including **(a-b)** straight channels, **(c)** serpentine channel used for long-term experiments, **(d)** straight channel with U-shaped contraction used for hydrodynamic orbiting of cells, **(e)** Flow-focusing system with an integrated expanded channel used for dynamic exchange of solutions, and **(f)** U-shaped channel used for mechanobiology experiment.

Supplementary Information 4: Pressure-volume curve for various balloon configurations

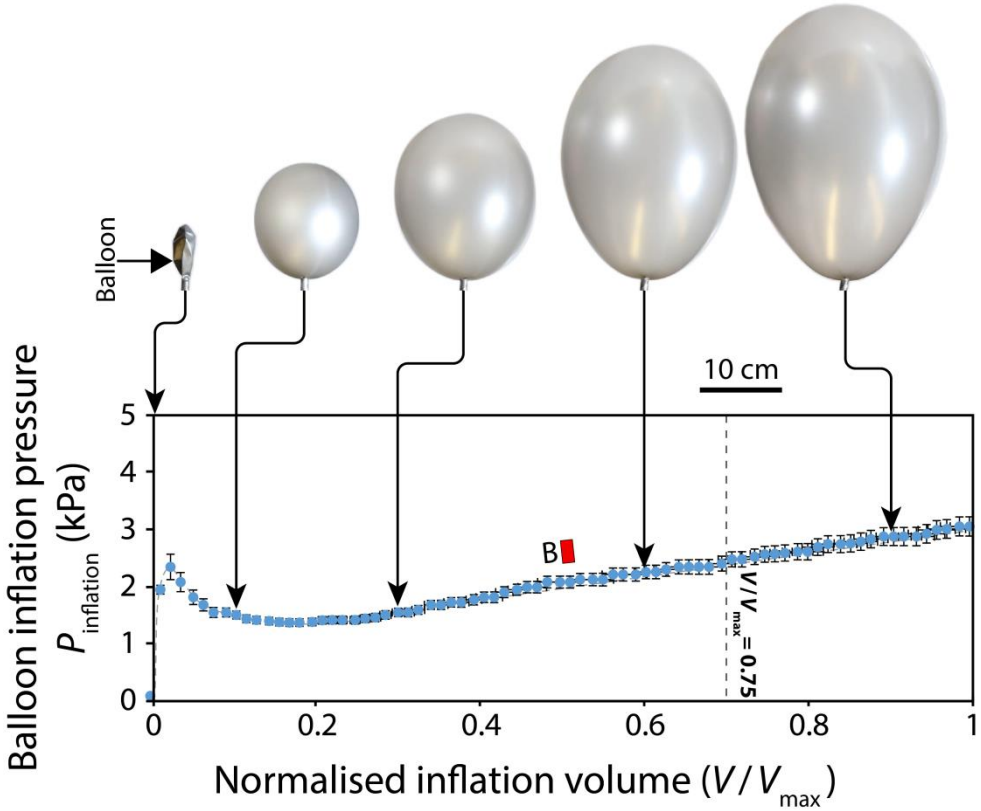

Figure S4a. Inflation pressure-normalised volume curve ($P_{inflation}$ *vs.* V/V_{max}) obtained for the **reference balloon**. Images show the expansion of the reference balloon at various pressures. Error bars represent average ± standard deviation obtained in three sets of independent experiments.

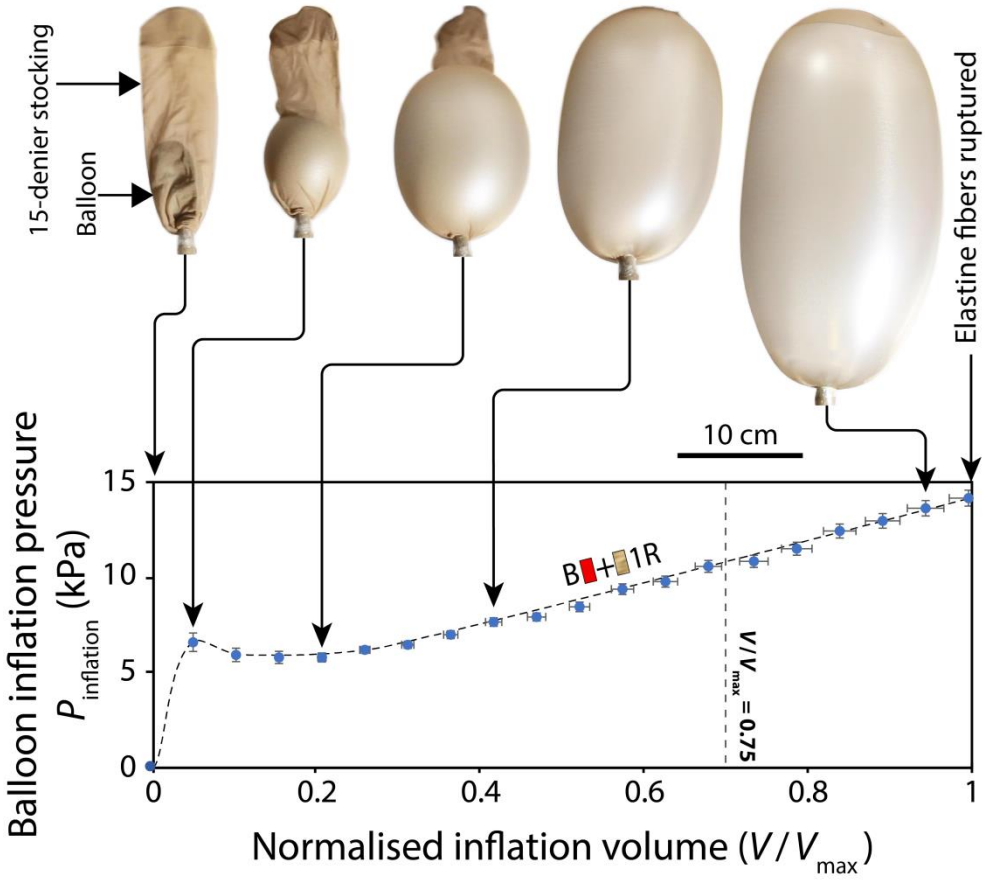

Figure S4b. Inflation pressure-normalised volume curve ($P_{inflation}$ *vs.* V/V_{max}) obtained for the **latex balloon reinforced with one layer of elastane fibres (B + 1R)** using a 15-denier stocking. Images show the expansion of the reinforced balloon at various pressures. Error bars represent average ± standard deviation obtained in three sets of independent experiments.

Appendix 1: Radius-inflation pressure curve of a latex balloon

The radius-inflation pressure curve of latex balloons is described using the spherical thin shell model [1-4], as given below:

$$P_{inflation} = P_{balloon} - P_{\infty} = \frac{2\,\gamma\,t_o}{r_o}\,k(\lambda)\left(\lambda^{-1} - \lambda^{-7}\right) \qquad (1)$$

where, P_{ballon} and P_{∞} are the internal balloon and ambient pressure, γ is the shear modulus of the latex, t_o and r_o are thickness and non-deformed radius of the balloon, $\lambda = r/r_o$ is the stretch ratio of the balloon, and $k(\lambda)$ is a dimensionless parameter, which according to the Mooney-Rivlin model [5] can be calculated as $k(\lambda) = 1 + \alpha\,\lambda^2$. The radius-inflation pressure curve of latex balloons has been investigated in detail in our previous work [6].

Supplementary Information 5: Comparing the volume of the reference and reinforced balloons

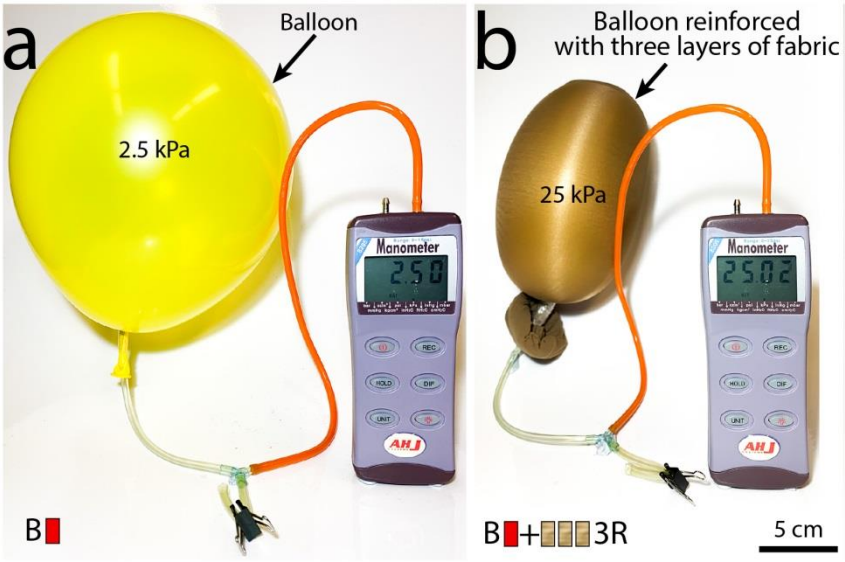

Figure S5. Comparing the volume of the reference and reinforced latex balloons. **(a)** The reference (non-reinforced) latex balloon inflated to $P_{\text{inflation}}$ = 2.5 kPa. **(b)**. The latex balloon reinforced with three layers of elastane fibres (B + 3R) inflated to $P_{\text{inflation}}$ = 25 kPa.

Supplementary Information 6: Variations of balloon inflation pressure and reinforcing coefficient versus the number of reinforcing layers

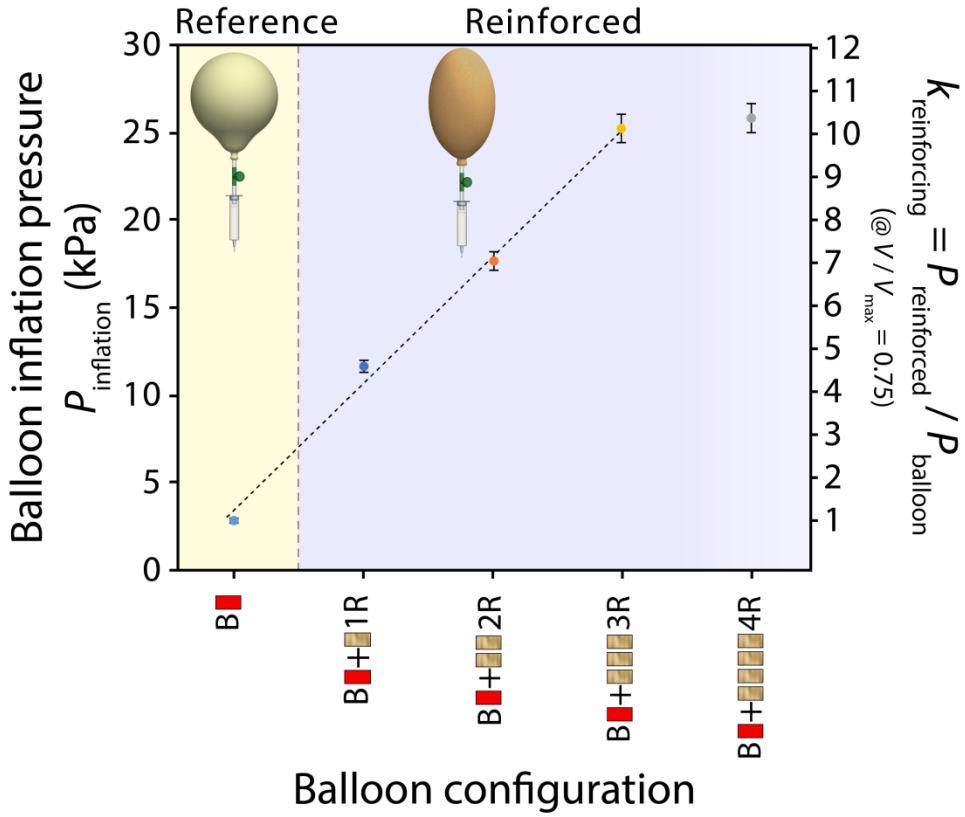

Figure S6. Variations of balloon inflation pressure and 'reinforcing coefficient' versus the number of reinforcing layers, obtained at $V/V_{max} = 0.75$. Error bars represent average±standard deviation obtained in three sets of independent experiments.

Supplementary Information 7: Pressure-volume curves of reinforced balloons obtained with various stocking brands

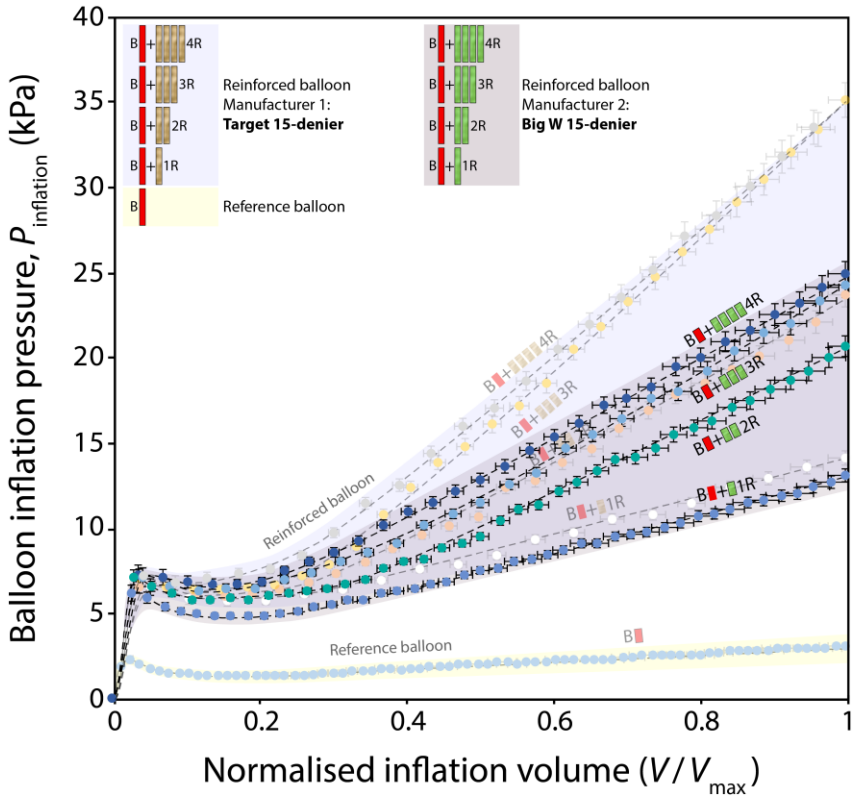

Figure S7. Pressure-normalised volume ($P_{inflation}$ *vs.* V/V_{max}) curves of reinforced balloons obtained with Big W 15-denier and Target 15-denier. Figure legend notation: B represents the latex balloon while R represents the reinforcing elastane layer. Error bars represent average ± standard deviation obtained in three sets of independent experiments.

Supplementary Information 8: Fatigue analysis of reinforced balloons over repeated inflations

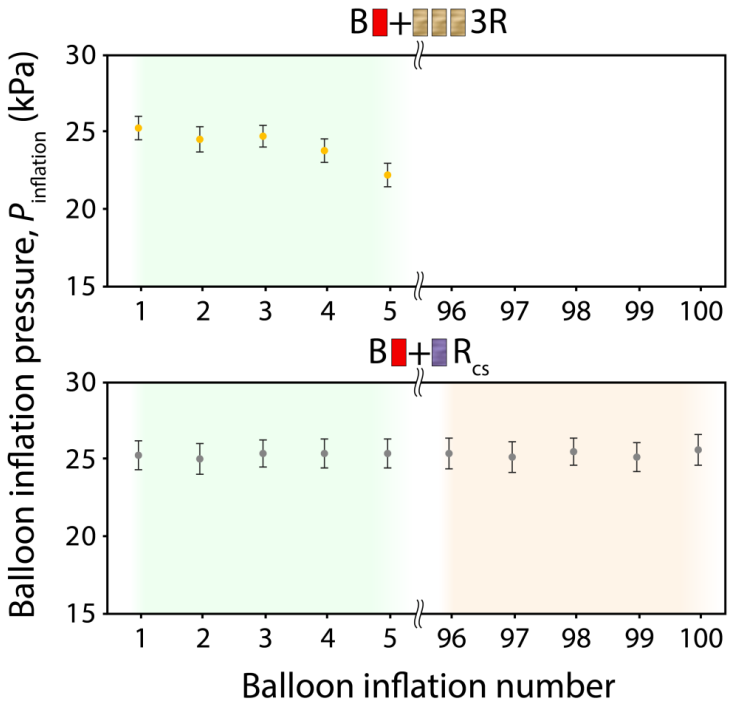

Figure S8a. Variations of balloon inflation pressure versus the number of inflations ($P_{inflation}$ *vs.* $N_{inflation}$), obtained for the reinforced balloons using three layers of elastane fibres (B + 3R) and compression socks (B + R_{cs}). Error bars represent average ± standard deviation obtained in five sets of independent experiments.

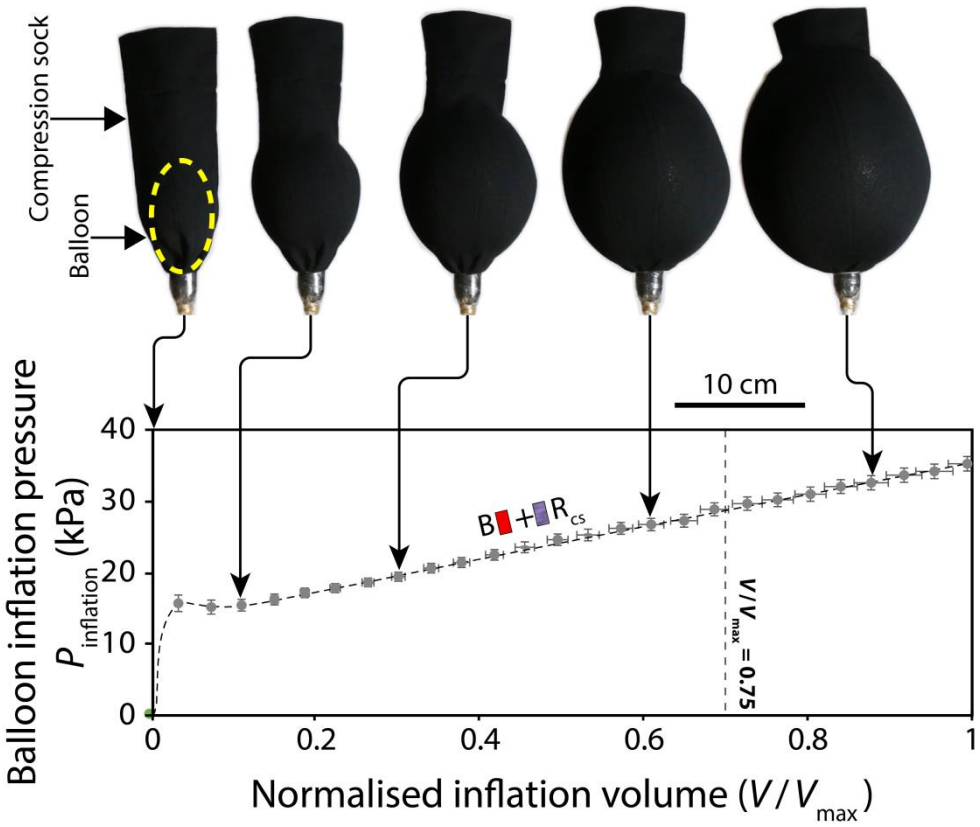

Figure S8b. Inflation pressure-normalised volume curve ($P_{inflation}$ *vs.* V/V_{max}) obtained for the **latex balloon reinforced with one layer of compression socks (B + 1R_{cs})**. Images show the expansion of the reinforced balloon at various pressures. Error bars represent average ± standard deviation obtained in three sets of independent experiments.

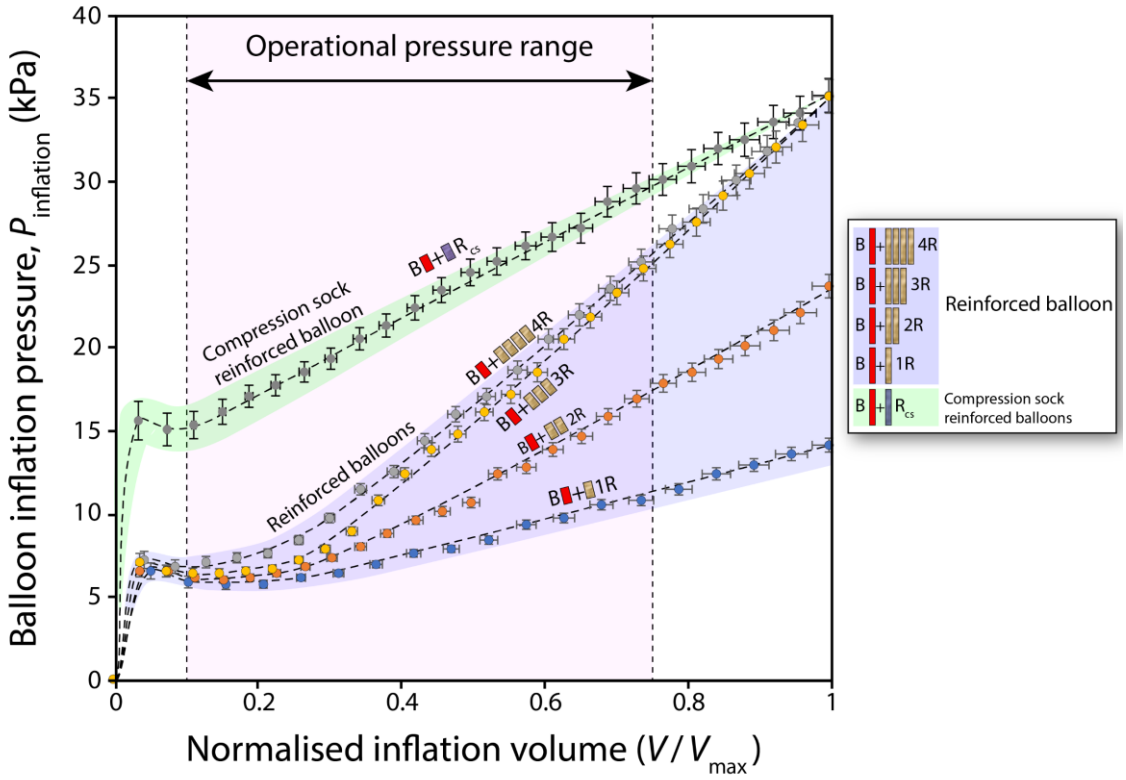

Figure S8c. Pressure-normalised volume ($P_{inflation}$ *vs.* V/V_{max}) curves of reinforced balloons obtained with stockings and compression socks. Figure legend notation: B represents the latex balloon while R represents the reinforcing elastane layer. Error bars represent average ± standard deviation obtained in three sets of independent experiments.

Supporting information 9: Pumping viscous liquids with the reinforced balloon pump

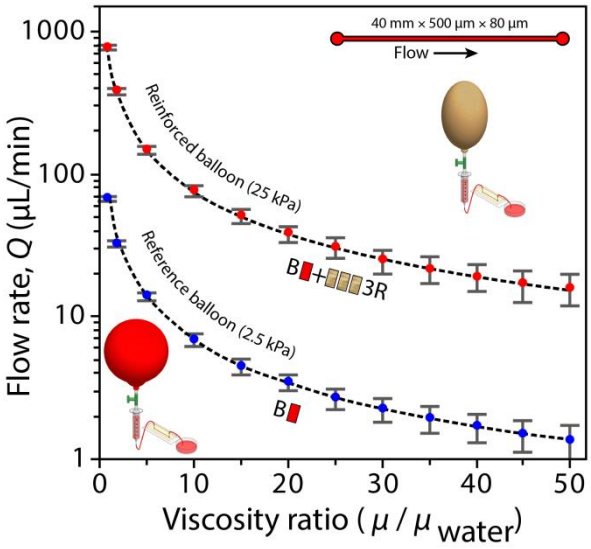

Figure S9. Liquid flow rate versus liquid viscosity ratio (Q *vs.* μ/μ_{water}). Viscosity is changed by using various volumetric ratios of glycerol to water. Liquid is driven through a straight microfluidic channel using reference and reinforced latex balloons. Error bars correspond to average ± standard deviation values obtained in three sets of independent experiments.

Appendix 2: Flow rate of liquid through the microfluidic system operated by a pressure pump

The liquid flow rate of the liquid through the microfluidic system operated by a pressure pump is set by the balloon inflation pressure and the viscous pressure drop along the system, as described below [6]:

$$P_{inflation} = P_{balloon} - P_{\infty} = \Delta P_{tubes} + \Delta P_{channel} = \frac{128\,\mu\,Q\,L_{tube}}{\pi\,D_{tube}^4} + \frac{k\,\mu\,Q\,L_{channel}}{W_{channel}\,H_{channel}^3} \qquad (2)$$

where, P_{ballon} and P_{∞} are the internal balloon and abmient pressure, μ is the liquid dynamic viscosity, Q is the liquid flow rate, L_{tube} and D_{tube} are the length and internal diameter of interconnecting Tygon® tubes at the inlet and outlet, k is a dimensionless parameter which depends on the aspect ratio of the microfluidic channel [7], and L_{channel}, W_{channel} and H_{channel} are the length, width and height of the microfluidic channel, respectively.

Supporting information 10: Instability patterns at the interface of two miscible liquids with a large viscosity contrast

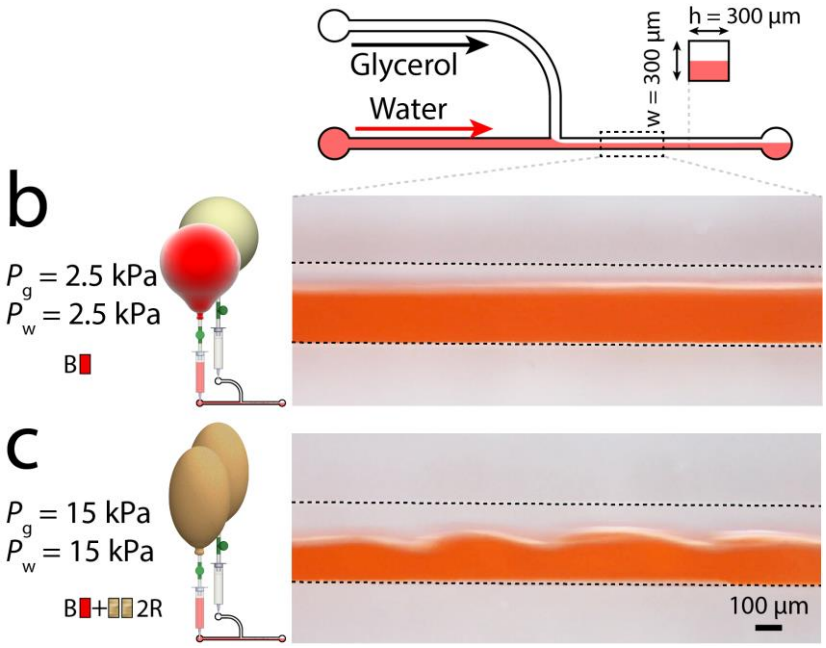

Figure S10. Instability patterns at the interface of water and glycerol due to a large viscosity contrast. ($\mu_{glycerol}$ = 1078.2 mPa.s, μ_{water} = 0.935 mPa.s) **(a)** Schematics of the microfluidic T-junction structure. **(b)** Laminar flow observed when operating the system with a pair of reference balloon pumps at $P_{inflation}$ = 2.5 kPa. **(c)** Instability patterns when operating the system with a pair of reinforced balloons (B + 2R) at $P_{inflation}$ = 15 kPa.

Supplementary Information 11: Increasing the generation rate of droplets using reinforced balloon pumps

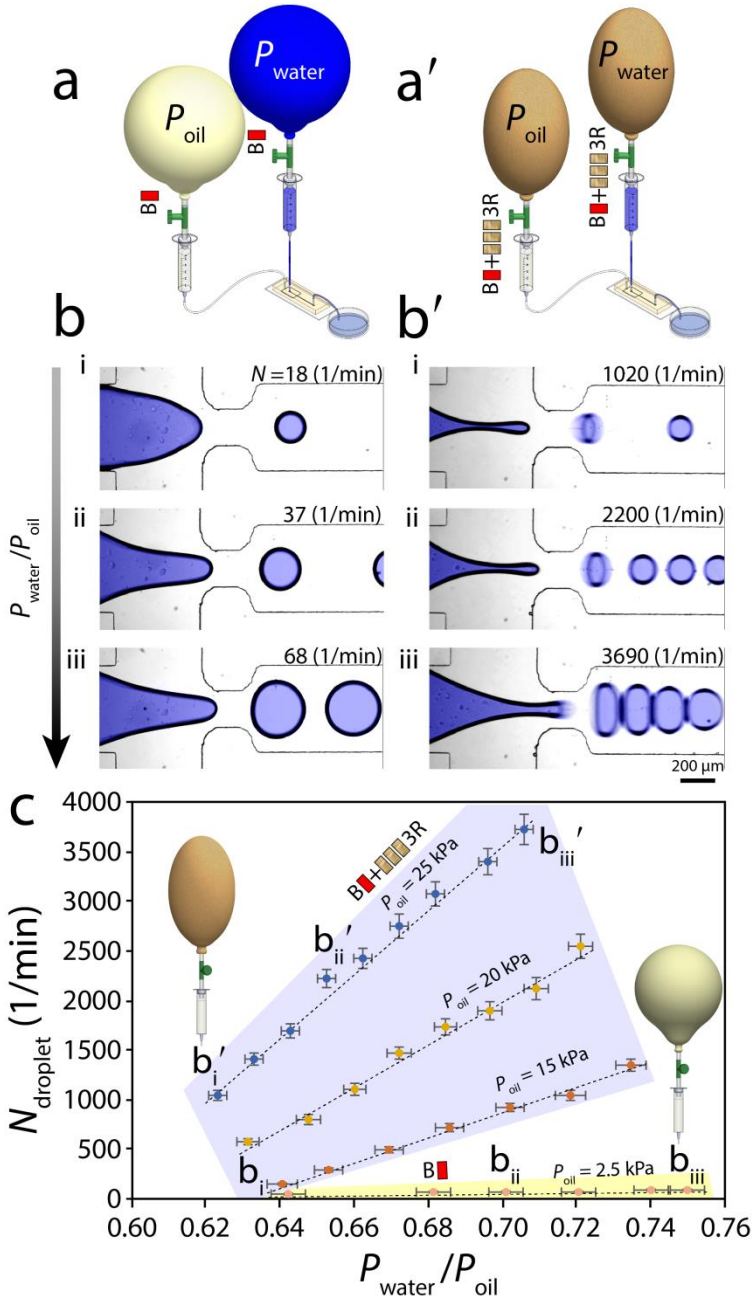

Figure S11. Increasing the generation rate of droplets through a flow focusing droplet generation system by implementing reinforced balloons pumps. Mineral oil (RTM8 oil, Sigma-Aldrich) with a viscosity of 10.37 mPa.s was used as the oil phase and water coloured with blue dye at a volumetric ratio of 20:1 with a viscosity of 0.93 mPa.s was used as the water phase: **(a-b)** Droplet generation using reference latex balloons operating at P_{oil} = 2.5 kPa and various P_{water}/P_{oil} ratios. **(a′-b′)** Droplet generation using reinforced latex balloons operating at P_{oil} = 25 kPa and various P_{water}/P_{oil} ratios. **(c)** Droplet generation rate versus water to oil pressure ratio ($N_{droplet}$ *vs.* P_{water}/P_{oil}) obtained by reference and reinforced latex balloons. Error bars represent average ± standard deviation obtained in four sets of independent experiments.

Table S1. Comparison of active pumping mechanisms common in microfluidic applications

Category	Pump type	Flow rate range [i]	Flow stability over time	Flow switching [ii] (dynamic flows)	Fabrication or maintenance requirement	Size	Liquid sensitive [iii]	Temperature sensitive	Bio-compatible	External power requirement	Low-power (battery operated)	Supporting equipment requirement	Cost	Suitability for point-of-care applications
Off-chip	**Syringe** [8, 9]	Low to High	Yes	Slow	No	Large	No	No	Yes	Yes	No	No	High	No
	Pressure [8]	Low to High	Yes	Rapid	No	Large	Yes	Yes	Yes	Yes	No	Yes	High	No
	Peristaltic [10, 11] [iv]	Low to High	Yes	Slow	No	Large	No	No	Yes	Yes	No	No	High	No
On-chip	**Pneumatic** [12-14]	Low	Yes	Rapid	Yes	Small	Yes	Yes	Yes	Yes	Yes	Yes	Low	Yes
	Piezoelectric [15-17]	Low to medium	Yes	Rapid	Yes [v]	Small	Yes	Yes	Yes	Yes	Yes	No	Low	Yes
	Diaphragm [18]	Low to medium	Yes	Rapid	No [vi]	Small	No	No	Yes	Yes	Yes	No	Low	Yes
	Centrifugal [19-21]	Low to medium	Yes	Rapid	Yes	Small	Yes	Yes	Yes	Yes	Yes	Yes	Low	Yes
	Surface tension driven [22, 23]	Medium to high	Yes	Rapid	No [vii]	Small	Yes	Yes	No [viii]	Yes	Yes	Yes	Low	No
	Electroosmotic [24-26]	Low	Yes	Rapid	No	Small	Yes	Yes	Yes	Yes	Yes	Yes	Low	Yes
	Acoustic [16, 27-29]	Low to medium	Yes	Rapid	Yes	Small	No	Yes	Yes	Yes	Yes	Yes	Low	Yes
	Electro-hydrodynamic [30-32]	Low to medium	Yes	Rapid	No	Small	Yes	No	No	Yes	Yes	No	Low	No
Current work	**Reinforced balloon pressure pump**	Low to medium	No [ix]	Rapid	No	Medium	Yes [x]	Yes [xi]	Yes	No	N/A	No	Extremely low	Yes

Notes:

i. Low flow rates are defined as $Q < 1$ mL/min, Medium flow rates are defined as $1 < Q < 10$ mL/min, High flow rate are defined as $Q > 10$ mL/min.

ii. Rapid here refers to dynamic response times in the order of millisecond.

iii. Being sensitive to liquid properties such as viscosity (pressure pumps), electrical conductivity (electro-hydrodynamic pumps), pH (electroosmotic, surface tension driven pumps).

iv. Peristaltic pumps are particularly suitable for recirculation of liquid for long-term experiments.

v. Commercially available miniaturised piezoelectric pumps are also available, as presented in [33].

vi. In this work [18], commercially available miniaturised diaphragm pumps have been utilised.

vii. The pumps referred to here are made of gallium based liquid metal alloys, which can be placed onto the desired locations of the system using a pipette.

viii. Liquid metal pumps release gallium ions to the solution.

ix. Pressure *vs* time curves are presented in Figure 2a.

x. Flow rate *vs* liquid viscosity curves are presented in Figure S9.

xi. Pressure *vs* temperature curves are presented in Figure 2d.

Supplementary Information 12: Variations of flow rate versus balloon inflation pressure through the microfluidic channel with a U-shaped contraction

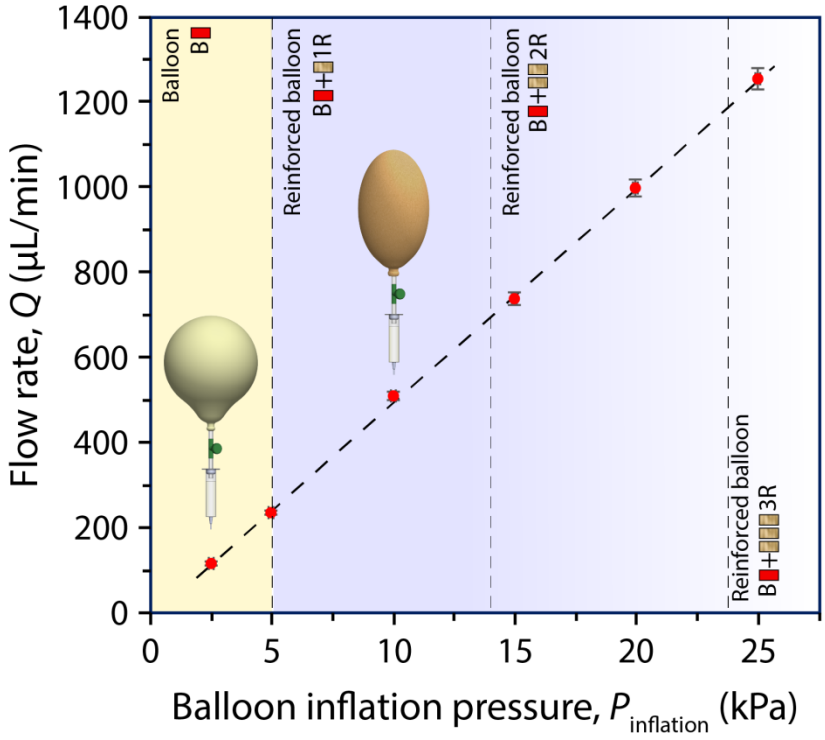

Figure S12. Variations of flow rate versus balloon inflation pressure (Q *vs.* $P_{inflation}$) through the microfluidic channel with a U-shaped contraction used for the hydrodynamic manipulation of human monocytes. Error bars represent average ± standard deviation obtained in five sets of independent experiments.

Supplementary Information 13: Microscopic imaging of large human monocytes

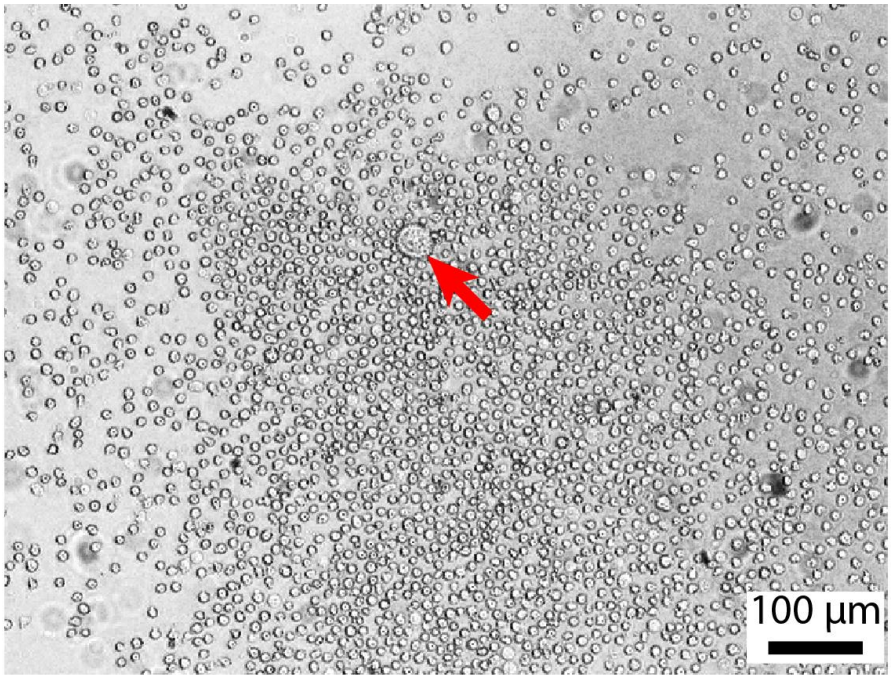

Figure S13. Microscopic images revealing the large size contrast between normal THP-1 monocytes (d_{cell} = 12.5 ± 1.4 µm) and large monocytes (d_{cell} = 40 ± 3.6 µm).

Supplementary Information 14: Lagrangian particle tracking model for the trajectory of human monocytes downstream of the U-shaped contraction

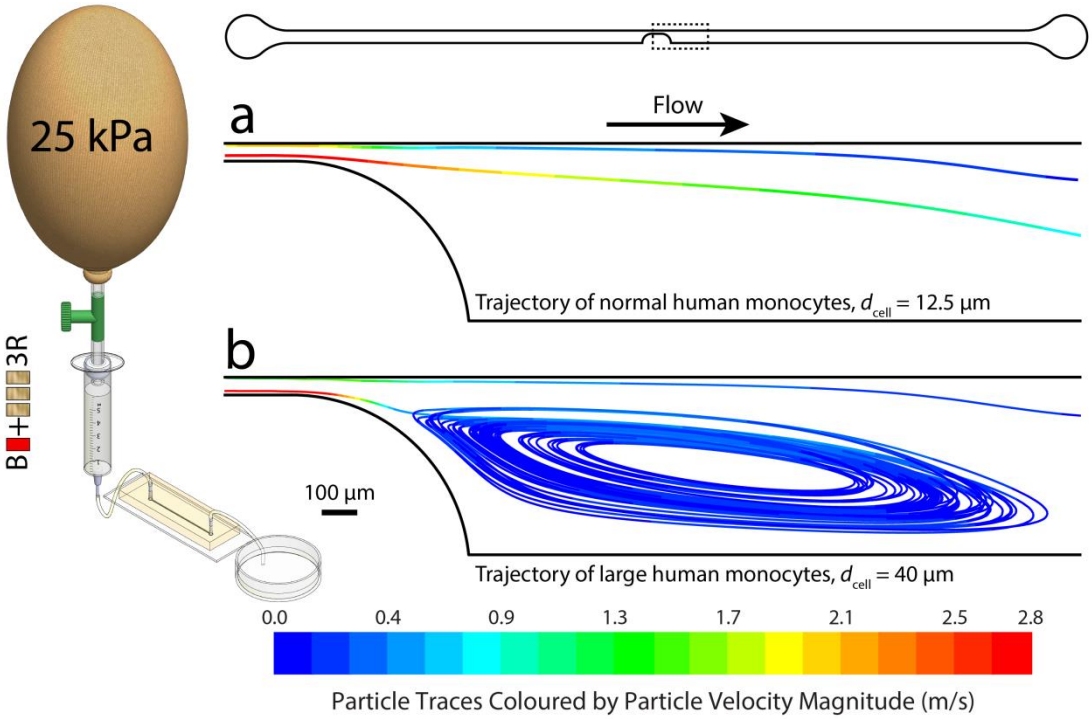

Figure S14. Flow streamlines at the downstream of the U-shaped contraction obtained by the Lagrangian particle tracking model. **(a)** Trajectory of normal THP-1 human monocytes (d_{cell} =12.5 µm). (**b)** Trajectory of large human monocytes (d_{cell} = 40 µm).

Supplementary Information 15: Characterisation of capturing performance of the vortex at various cell concentrations

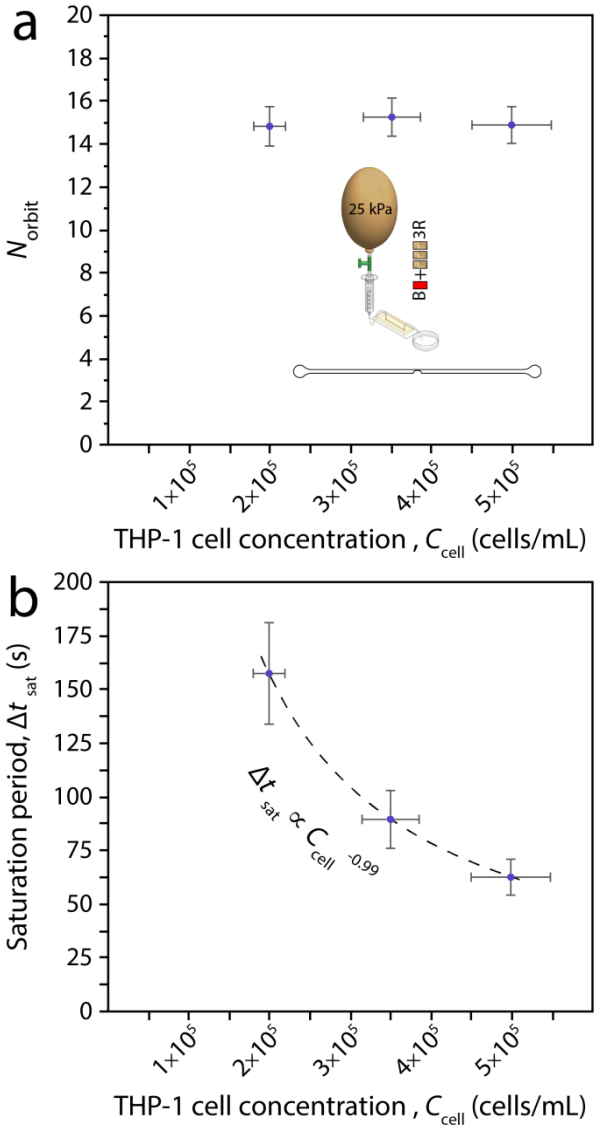

Figure S15. The cell vortex saturation characteristics of our microfluidic system. **(a)** Variations of the maximum number of captured cells against cell concentration (N_{orbit} *vs.* C_{cell}). **(b)** Variations of the vortex saturation period against cell concentration (Δt_{sat} *vs.* C_{cell}). Error bars represent average ± standard deviation obtained in five sets of independent experiments.

Supplementary Information 16: Laminar flow of neighbouring red and blow streams at low pressures

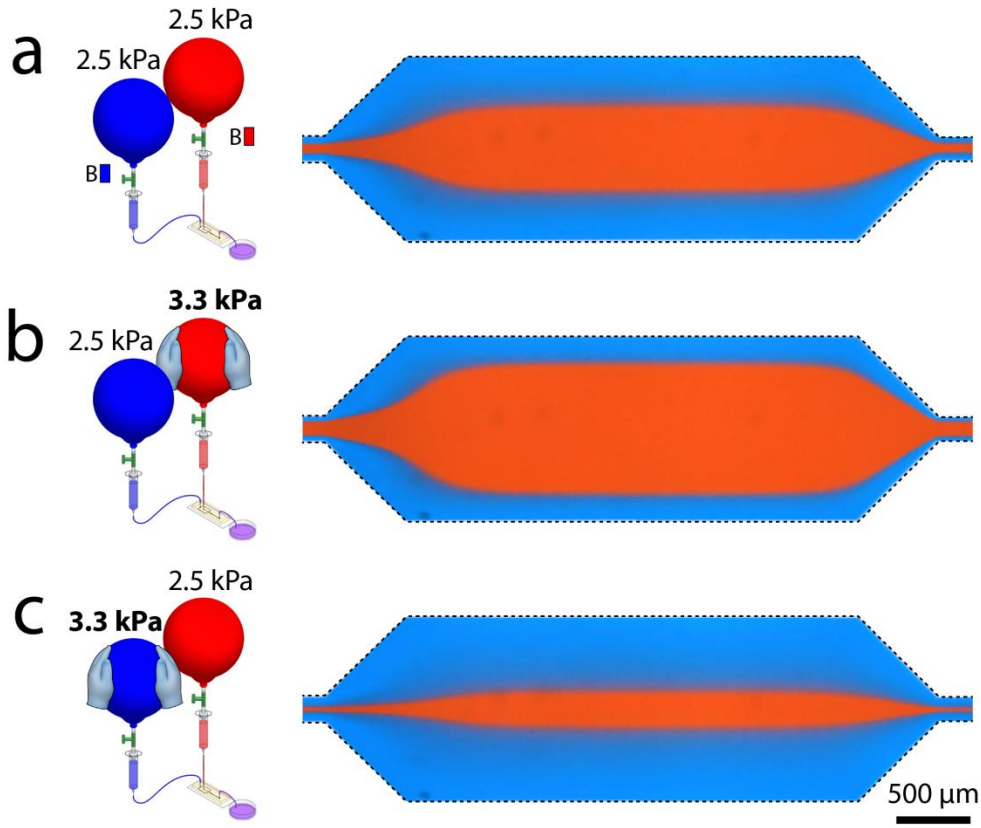

Figure S16a. Laminar flow of miscible red and blue flow using a pair of reference balloons at $P_{\text{inflation}}$ = 2.5 kPa **obtained by experiments**: **(a)** Static conditions. **(b)** Expanded core flow by manually squeezing of the red balloon. **(c)** Narrowed core flow by manually squeezing of the blue balloon.

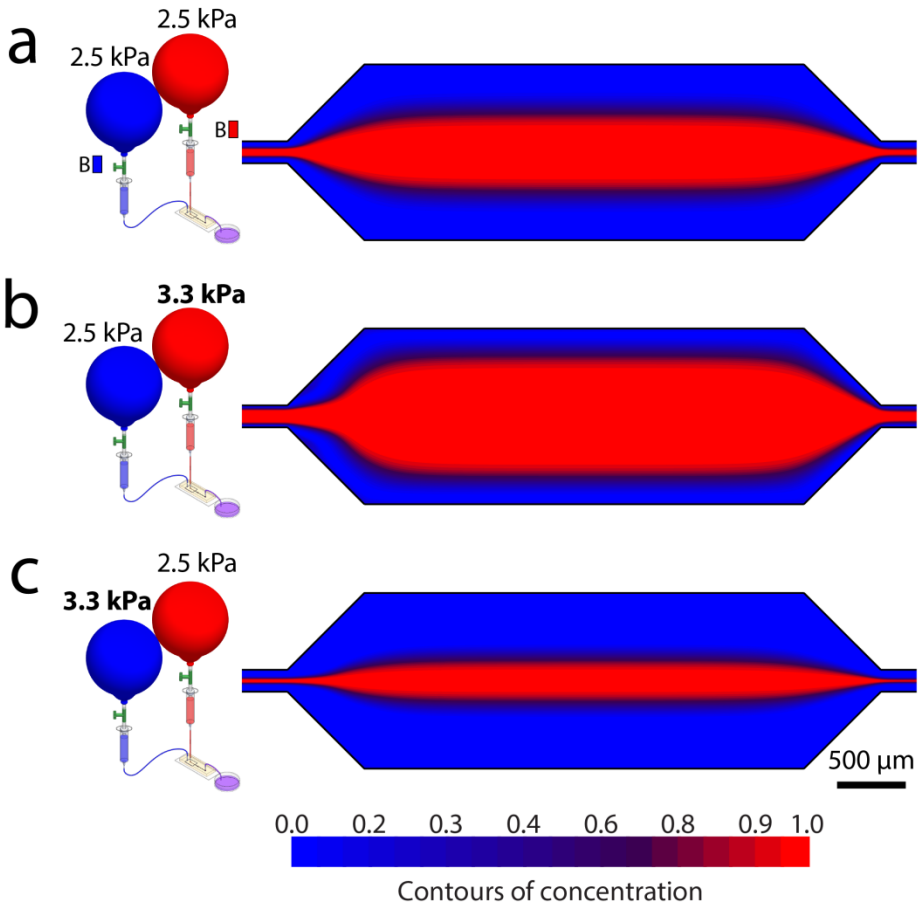

Figure S16b. Laminar flow of miscible red and blue flow using a pair of reference balloons at $P_{\text{inflation}}$ = 2.5 kPa **obtained by numerical simulations**: **(a)** Reference mode. **(b)** Expanded core flow by increasing the inflation pressure of the red balloon. **(c)** Narrowed core flow by increasing the inflation pressure of the blue balloon.

Supplementary Information 17: Vortex formation at the expanded channel at high inflation pressures

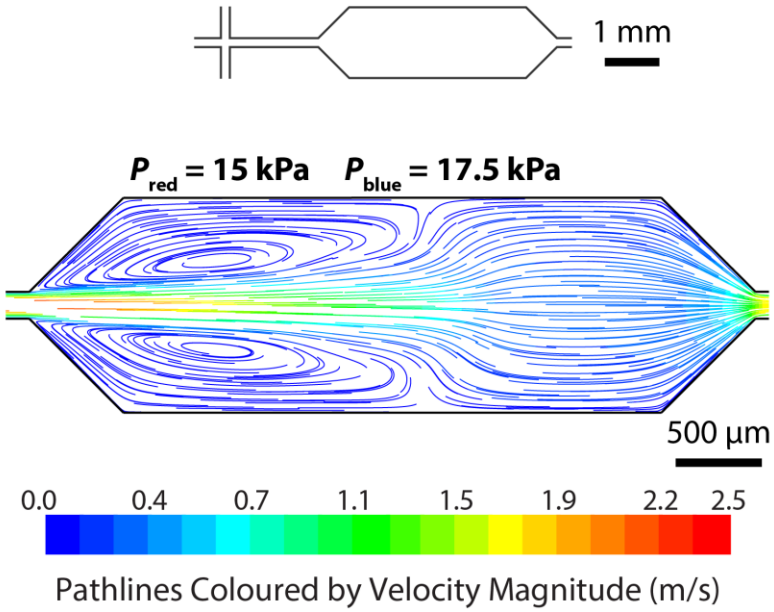

Figure S17. Flow streamlines obtained by numerical simulations revealing the formation of vortices at the expanded channel at high inflation pressures using reinforced balloons.

Supplementary Information 18: Dynamic pressure changes obtained by manually squeezing a reinforced balloon

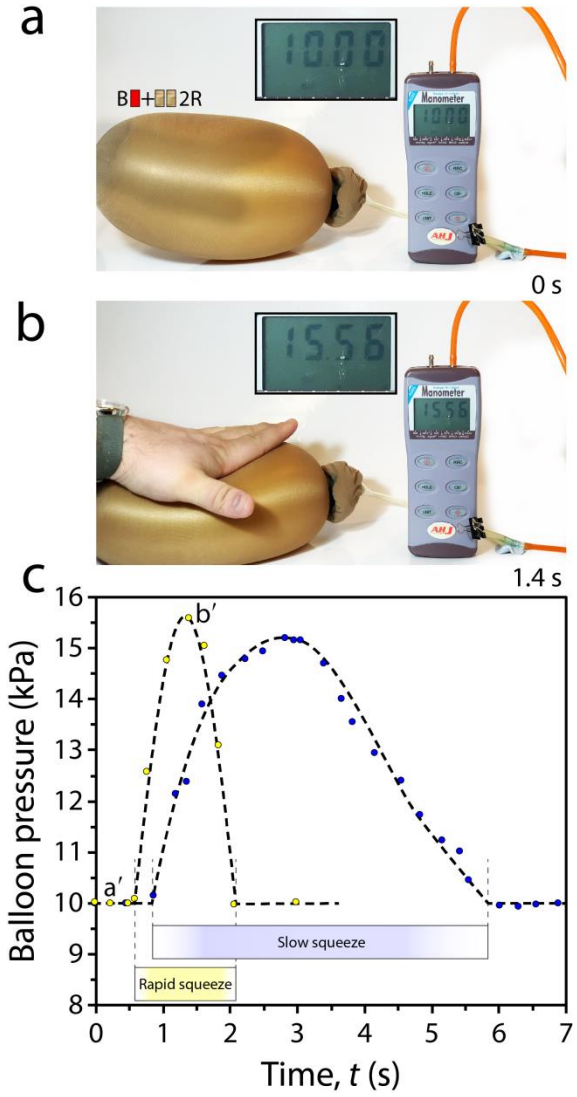

Figure S18. Dynamic pressure changes of a reinforced balloon following manual squeezing. **(a-b)** A reinforced balloon before and after manual squeezing with a digital pressure gauge. **(c)** The dynamic pressure curves obtained by various squeezing patterns.

Supplementary Information 19: Concentration profiles of red and blue flows through the flow focusing systems

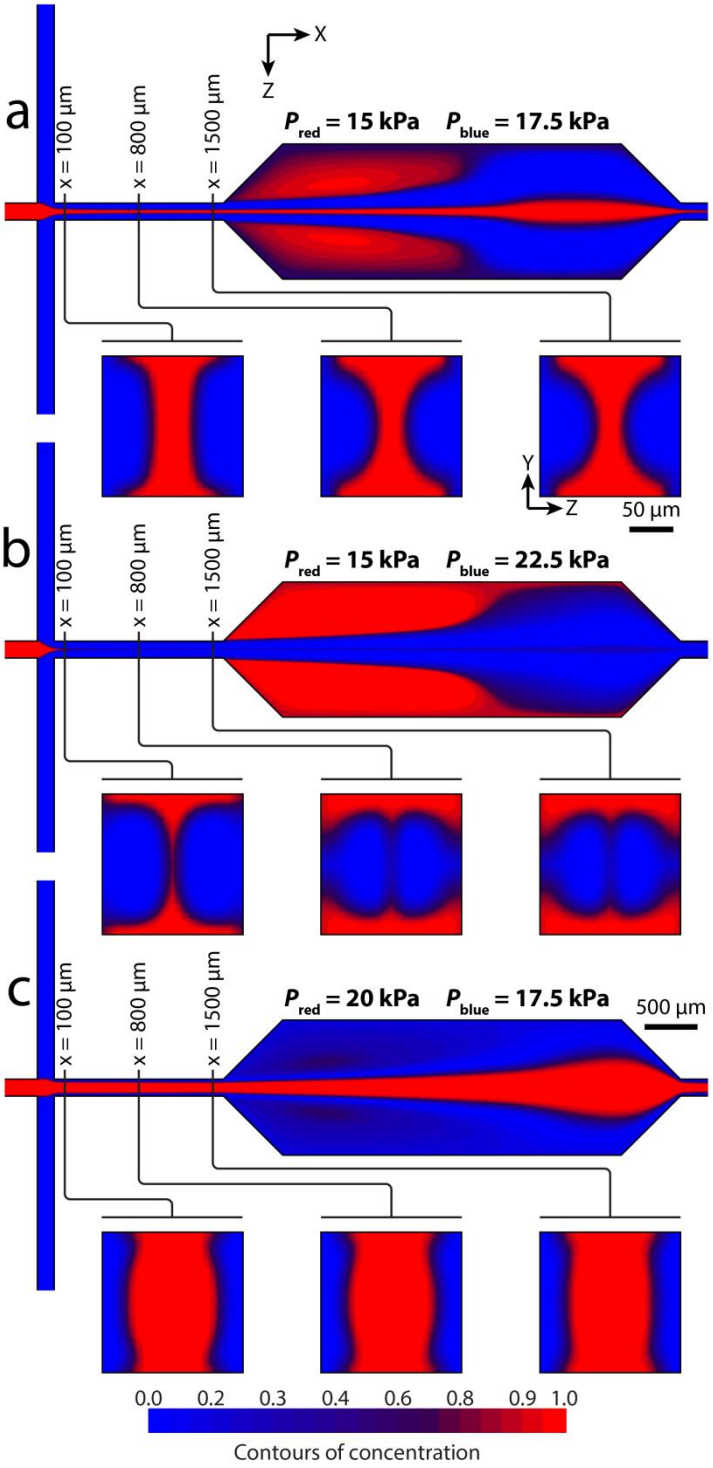

Figure S19a. **Top-view** concentration profile of red and blue flows through the flow focusing system obtained by numerical simulations at high inflation pressures: **(a)** Reference mode: P_{red} = 15 kPa, P_{blue} = 17.5 kPa. **(b)** Narrowed core flow: P_{red} = 15 kPa, P_{blue} = 22.5 kPa. **(c)** Expanded core flow: P_{red} = 20 kPa, P_{blue} = 17.5 kPa. With insets showing the cross sections of the channel prior to the expansion.

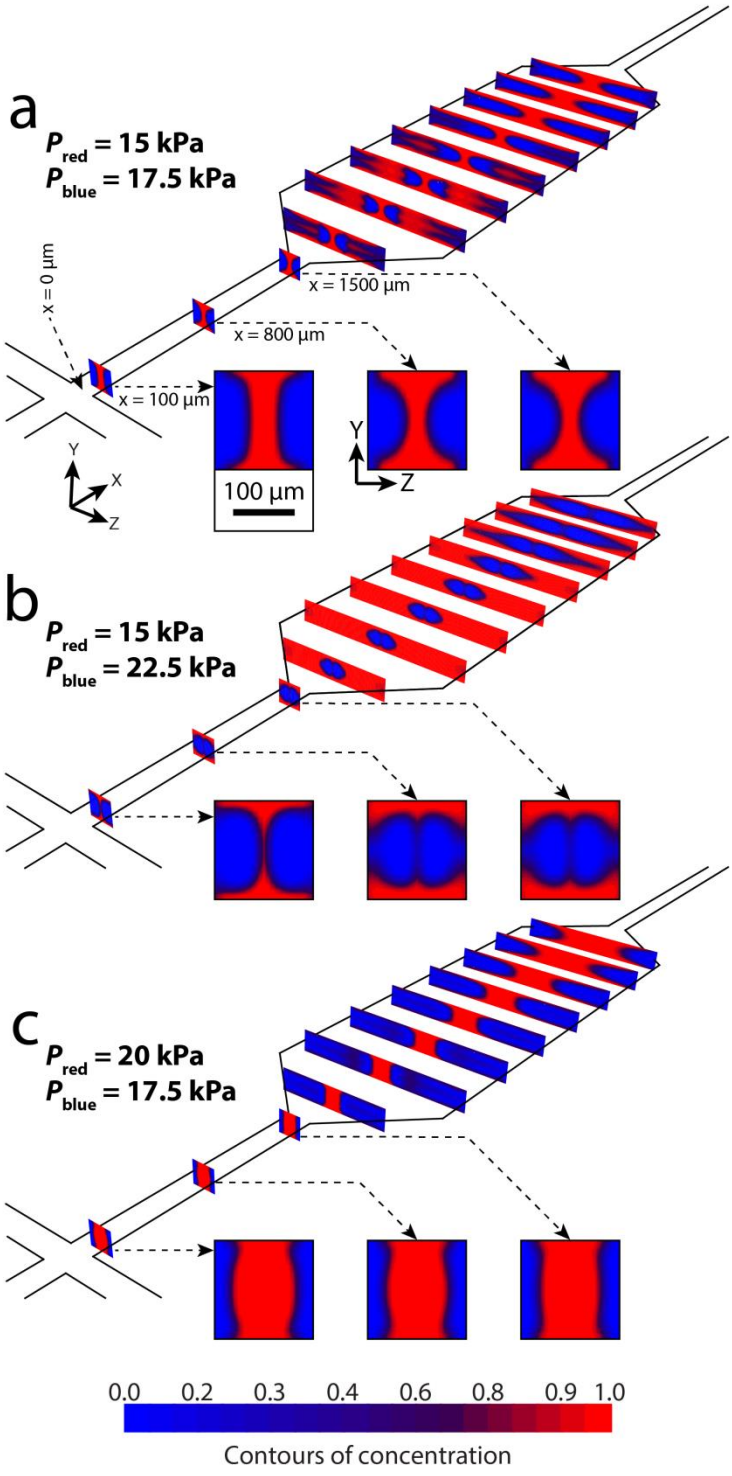

Figure S19b. **Isometric-view** concentration profile of red and blue flows through the flow focusing system obtained by numerical simulations at high inflation pressures: **(a)** Reference mode: P_{red} = 15 kPa, P_{blue} = 17.5 kPa. **(b)** Narrowed core flow: P_{red} = 15 kPa, P_{blue} = 22.5 kPa. **(c)** Expanded core flow: P_{red} = 20 kPa, P_{blue} = 17.5 kPa. With insets showing the cross sections of the channel prior to the expansion.

Supplementary Information 20: Rapid exchange of solutions enabled by the manual squeezing of a reinforced balloon

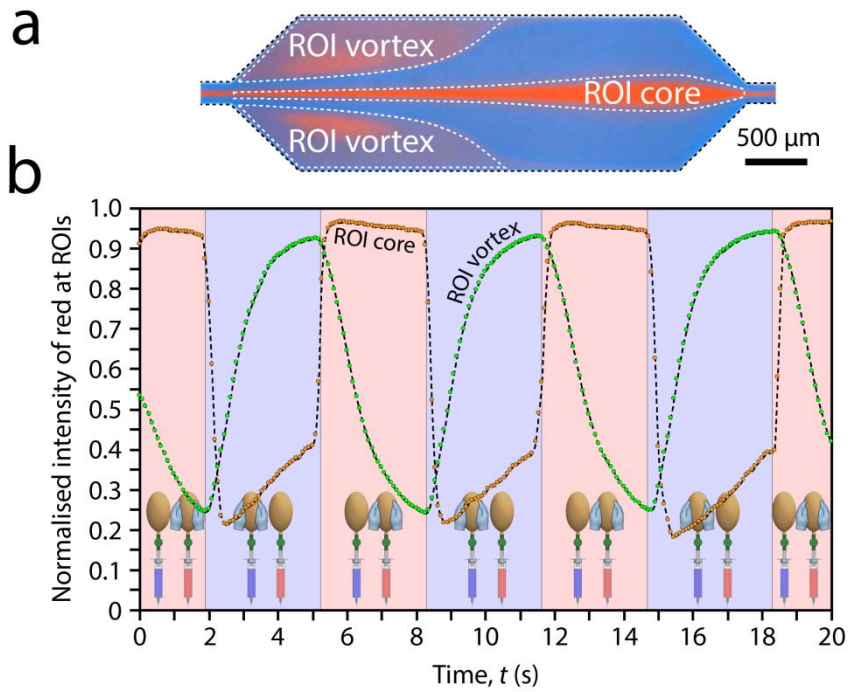

Figure S20. Rapid exchange of solutions within an expanded channel downstream of a flow focusing system enabled by the manual squeezing of a reinforced balloon. **(a)** The regions of interests (ROIs) for the vortices and core flow. **(b)** The normalised mean intensity of the red channel at the vortex and core ROIs extracted using ImageJ over time.

Supplementary Information 21: Investigating the mechanobiology of endothelial cells under shear stress using reinforced balloon pumps

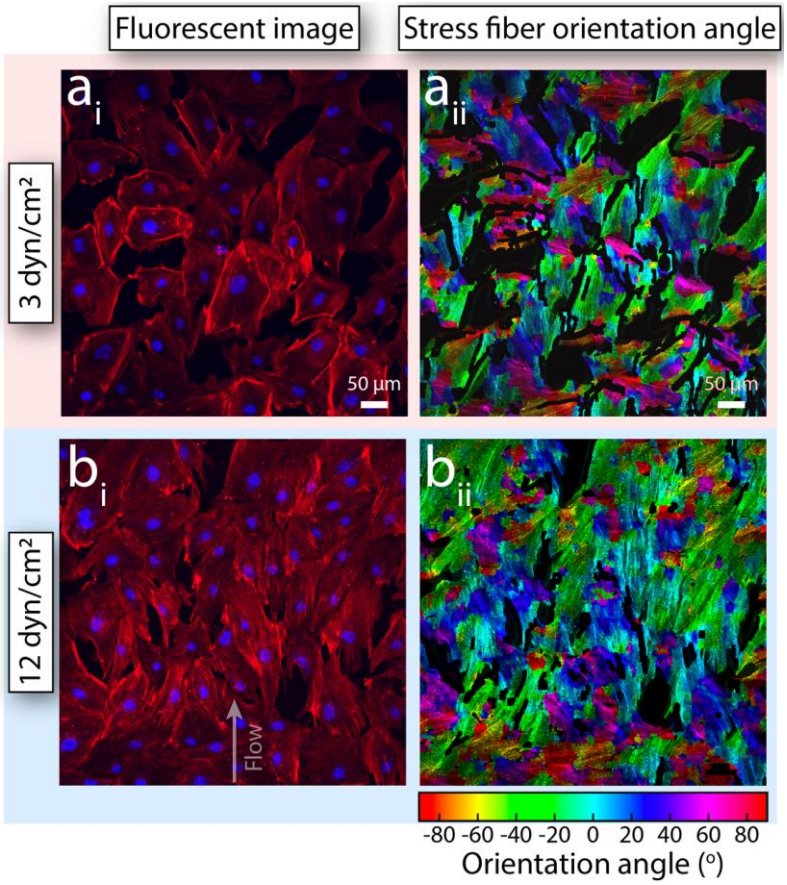

Figure S22. Investigating the mechanobiology of HAECs under shear stress utilising a reinforced balloon pump: **(a_i-b_i)** Fluorescent micrograph of HAECs following 9 hours of stimulation under low (3 dyne/cm^2) and high (12 dyne/cm^2) shear stress conditions, **(a_{ii}-b_{ii})** Coloured contours of stress fiber orientation angle.

References:

1 L. M. Kanner and C. O. Horgan, *Int J Non Linear Mech*, 2007, **42**, 204-215.
2 R. Mangan and M. Destrade, *Int J Non Linear Mech*, 2015, **68**, 52-58.
3 A. Needleman, *Int J Solids Struct*, 1977, **13**, 409-421.
4 I. Müller and H. Struchtrup, *Math Mech Solids*, 2002, **7**, 569-577.
5 M. Mooney, *J Appl Phys*, 1940, **11**, 582-592.
6 P. Thurgood, J. Y. Zhu, N. Nguyen, S. Nahavandi, A. R. Jex, E. Pirogova, S. Baratchi and K. Khoshmanesh, *Lab Chip*, 2018, **18**, 2730-2740.
7 M. J. Fuerstman, A. Lai, M. E. Thurlow, S. S. Shevkoplyas, H. A. Stone and G. M. Whitesides, *Lab Chip*, 2007, **7**, 1479-1489.
8 T. Ward, M. Faivre, M. Abkarian and H. A. Stone, *Electrophoresis*, 2005, **26**, 3716-3724.
9 S. Baratchi, F. J. Tovar-Lopez, K. Khoshmanesh, M. S. Grace, W. Darby, J. Almazi, A. Mitchell and P. McIntyre, *Biomicrofluidics*, 2014, **8**, 044117.
10 F. Tovar-Lopez, P. Thurgood, C. Gilliam, N. Nguyen, E. Pirogova, K. Khoshmanesh and S. Baratchi, *Front Bioeng Biotechnol*, 2019, **7**.
11 D. M. Lewis, N. Mavrogiannis, Z. Gagnon and S. Gerecht, *Biomicrofluidics*, 2018, **12**, 042202.
12 Y.-S. Lee, N. Bhattacharjee and A. Folch, *Lab Chip*, 2018, **18**, 1207-1214.
13 A. Pourmand, S. A. M. Shaegh, H. B. Ghavifekr, E. Najafi Aghdam, M. R. Dokmeci, A. Khademhosseini and Y. S. Zhang, *Sens Actuators B Chem*, 2018, **262**, 625-636.
14 C. Szydzik, A. F. Gavela, S. Herranz, J. Roccisano, M. Knoerzer, P. Thurgood, K. Khoshmanesh, A. Mitchell and L. M. Lechuga, *Lab Chip*, 2017, **17**, 2793-2804.
15 P.-H. Cazorla, O. Fuchs, M. Cochet, S. Maubert, G. Le Rhun, Y. Fouillet and E. Defay, *Sens Actuators A Phys*, 2016, **250**, 35-39.
16 Y. Lin, C. Gao, Y. Gao, M. Wu, A. Ahmadian Yazdi and J. Xu, *Sens Actuators B Chem*, 2019, **287**, 312-319.
17 Z. Cheng, X. Wu, J. Cheng and P. Liu, *Microfluid Nanofluidics*, 2017, **21**, 9.
18 K. A. Addae-Mensah, Y. K. Cheung, V. Fekete, M. S. Rendely and S. K. Sia, *Lab Chip*, 2010, **10**, 1618-1622.
19 S. Asiaei, S. Fakhari, E. Pishbin, F. Ghorbani-Bidkorbeh, M. Eghbal and M. Navidbakhsh, *J Micromech Microeng*, 2019, **29**, 075001.
20 F. Stumpf, F. Schwemmer, T. Hutzenlaub, D. Baumann, O. Strohmeier, G. Dingemanns, G. Simons, C. Sager, L. Plobner, F. von Stetten, R. Zengerle and D. Mark, *Lab Chip*, 2016, **16**, 199-207.
21 H. V. Nguyen, V. D. Nguyen, E. Y. Lee and T. S. Seo, *Biosens Bioelectron*, 2019, **136**, 132-139.
22 S.-Y. Tang, K. Khoshmanesh, V. Sivan, P. Petersen, A. P. O'Mullane, D. Abbott, A. Mitchell and K. Kalantar-zadeh, *Proc Natl Acad Sci USA*, 2014, **111**, 3304-3309.
23 J. Y. Zhu, P. Thurgood, N. Nguyen, K. Ghorbani and K. Khoshmanesh, *Lab Chip*, 2017, **17**, 3862-3873.
24 Z. Ye, R. Zhang, M. Gao, Z. Deng and L. Gui, *Micromachines*, 2019, **10**, 112.
25 X. Gao and Y. X. Li, *J Appl Phys*, 2018, **123**, 164301.
26 M. Vázquez Piñón, B. Cárdenas Benítez, B. Pramanick, V. H. Perez-Gonzalez, M. J. Madou, S. O. Martinez-Chapa and H. Hwang, *Sens Actuators A Phys*, 2017, **262**, 10-17.
27 J. Friend and L. Y. Yeo, *Rev Mod Phys*, 2011, **83**, 647-704.
28 A. R. Tovar, M. V. Patel and A. P. Lee, *Microfluid Nanofluidics*, 2011, **10**, 1269-1278.
29 R. Rimsa, A. J. Smith, C. Wälti and C. D. Wood, *Appl Phys Lett*, 2017, **111**, 234102.
30 M. K. Russel, S. M. Hasnain, P. R. Selvaganapathy and C. Y. Ching, *Microfluid Nanofluidics*, 2016, **20**, 112.
31 Y. Li, Y. Ren, W. Liu, X. Chen, Y. Tao and H. Jiang, *Electrophoresis*, 2017, **38**, 983-995.
32 S. K. Tadavani, J. R. Munroe and A. Yethiraj, *Soft Matter*, 2016, **12**, 9246-9255.
33 J. Akagi, K. Khoshmanesh, C. J. Hall, J. M. Cooper, K. E. Crosier, P. S. Crosier and D. Wlodkowic, *Sens Actuators B Chem*, 2013, **189**, 11-20.